Modulating inner Helmholtz layer by electrocatalytically sieving $[Zn(H_2O)_6]^{2+}$ for 10000-cycle zinc-ion hybrid capacitors under extremely harsh conditions

Ziling Wu [a], Yinze Zuo [b], Yongzheng Zhang [a,*], Xiang Li [a], Jing Zhang [d], Yanli Wang [a], Chunyin Shen [a], Xiaomin Cheng [c], Meinan Liu [e], Haitao Liu [f], Hongzhen Lin [c], Jian Wang [c,g,h,**], Liang Zhan [a,*], Licheng Ling [a]

[a] *State Key Laboratory of Green Chemical Engineering and Industrial Catalysis, Key Laboratory of Specially Functional Polymeric Materials and Related Technology (Ministry of Education), State Key Laboratory of Chemical Engineering, East China University of Science and Technology, Shanghai 200237, China*
[b] *Institute of New Energy Materials and Engineering, College of Materials Science and Engineering, Fuzhou University, Fuzhou 350108, China*
[c] *i-Lab & CAS Key Laboratory of Nanophotonic Materials and Device Suzhou Institute of Nano-Tech and Nano-Bionics, Chinese Academy of Sciences, Suzhou, Jiangsu 215123, China*
[d] *School of Materials Science and Engineering, Xi'an University of Technology, Xi'an 710048, China*
[e] *State Key Laboratory of Featured Metal Materials and Life-Cycle Safety for Composite Structures, School of Resource, Environments and Materials, Guangxi University, Nanning 530004, China*
[f] *Institute of Applied Physics and Computational Mathematics, National Key Laboratory of Computational Physics, Beijing 100088, China*
[g] *Helmholtz Institute Ulm (HIU), Ulm D-89081, Germany*
[h] *Karlsruhe Institute of Technology (KIT), Karlsruhe D-76021, Germany*

Keywords:
Zinc-ion hybrid capacitor
Inner Helmholtz plane
Desolvation kinetics
Electrocatalytic sieving
Extreme environment

A B S T R A C T

Zinc-ion hybrid capacitors (ZIHCs) are famous for potential applications in grid-scale energy storage devices with fast-charge capability. However, their industrialization is severely plagued by inferior performance caused by the sluggish Zn^{2+} desolvation kinetics with large spatial diffusion hinderance of $[Zn(H_2O)_6]^{2+}$ in the inner Helmholtz plane (IHP) layer, especially under low-temperature surroundings. Herein, the simultaneous rapid desolvation strategy *via* pore sieving and electrocatalysis is initially proposed to promote $[Zn(H_2O)_6]^{2+}$ dissociation, regulating the isolated Zn^{2+} behaviors in the IHP. Specifically, heteroatom-decorated carbon microspheres with multi-level channels modulate the local distribution of electronic density, generating abundant catalytic sites to drive the kinetics of $[Zn(H_2O)_6]^{2+}$ desolvation and free Zn^{2+} diffusion. Impressively, the catalytic desolvation behaviors and storage mechanism of ZIHCs are comprehensively investigated using *in-situ* electrochemical quartz crystal microbalance and various *ex-situ/in-situ* measurements as well as theoretical simulations, revealing significant interactions of isolated Zn^{2+} in the IHP. Consequently, the assembled ZIHCs exhibit a superior capacity of 177.2 mAh g^{-1}, corresponding to a high energy density of 158.8 Wh kg^{-1}, and provide a power density as high as 15.7 kW kg^{-1}. Exposed to extreme environment, the ZIHCs encountered with severe solvation structure stabilize for 10000 cycles withcapacity retention of 99.42%, providing new insights of catalytically sieving into modulating IHP for high-performance ZIHCs under extreme conditions.

1. Introduction

The exploitation of renewable energy sources has faced severe challenges of intermittent production and uneven geographical distribution, urgently requiring high-performance energy storage systems [1–3]. Aqueous zinc-ion hybrid capacitors (ZIHCs) are regarded as one of the promising energy storage devices owing to their high power density and long lifespan with high safety [4,5]. Unfortunately, the

* Corresponding authors.
** Corresponding author at: i-Lab & CAS Key Laboratory of Nanophotonic Materials and Device Suzhou Institute of Nano-Tech and Nano-Bionics, Chinese Academy of Sciences, Suzhou, Jiangsu 215123, China.
E-mail addresses: zhangyongzheng@ecust.edu.cn (Y. Zhang), jian.wang@kit.edu (J. Wang), zhanliang@ecust.edu.cn (L. Zhan).

electrochemical performance of ZIHCs differs greatly from expectations due to the kinetics impedance in the inner Helmholtz plane (IHP) layer at the electrode/electrolyte interface, resulting from severe solvation shell of $[Zn(H_2O)_6]^{2+}$, sluggish ion diffusion, and depressive Zn^{2+} adsorption in the electrode [6,7].

To tackle the aforementioned challenges, different strategies have been employed to enhance the performance of ZIHCs, including: pore designing [8], defect engineering [9], interfacial modifying [10] and heteroatom doping [11]. Although encouraging progresses have been achieved, above strategies are designed in random without idealism, and these efforts have not yet met the practical demands in rate capability and cycling stability [12]. The depressive performances should be ascribed to the difficulty in realizing the water-free Zn^{2+} carrier [13]. As well known, the large-size cohesive $[Zn(H_2O)_6]^{2+}$ is formed by strong electrostatic coordination interaction between free Zn^{2+} and H_2O molecules, and increases the diffusion barrier from the electrolyte into the interior of the electrode, leading to sluggish kinetics at the cathode and unsatisfactory Zn^{2+} storage, especially at low temperatures [14–16]. Therefore, regulating the solvation behaviors of $[Zn(H_2O)_6]^{2+}$ at the interface is strongly required for affording the isolated Zn^{2+}.

As known, the inner structure of electric double layer on the electrode is regarded as the IHP layer, and the solvated Zn^{2+} is not allowed in the nanoscale-level IHP. Interfacial desolvation has aroused increasing attention for high-performance energy storage systems, which plays a prerequisite and rate-determining step for later diffusion, adsorption and reaction [17–20]. Fortunately, significant effort has been made in electrolyte strategy to regulate the solvation structure of Zn^{2+}, including high-concentration salts, functional additives, and

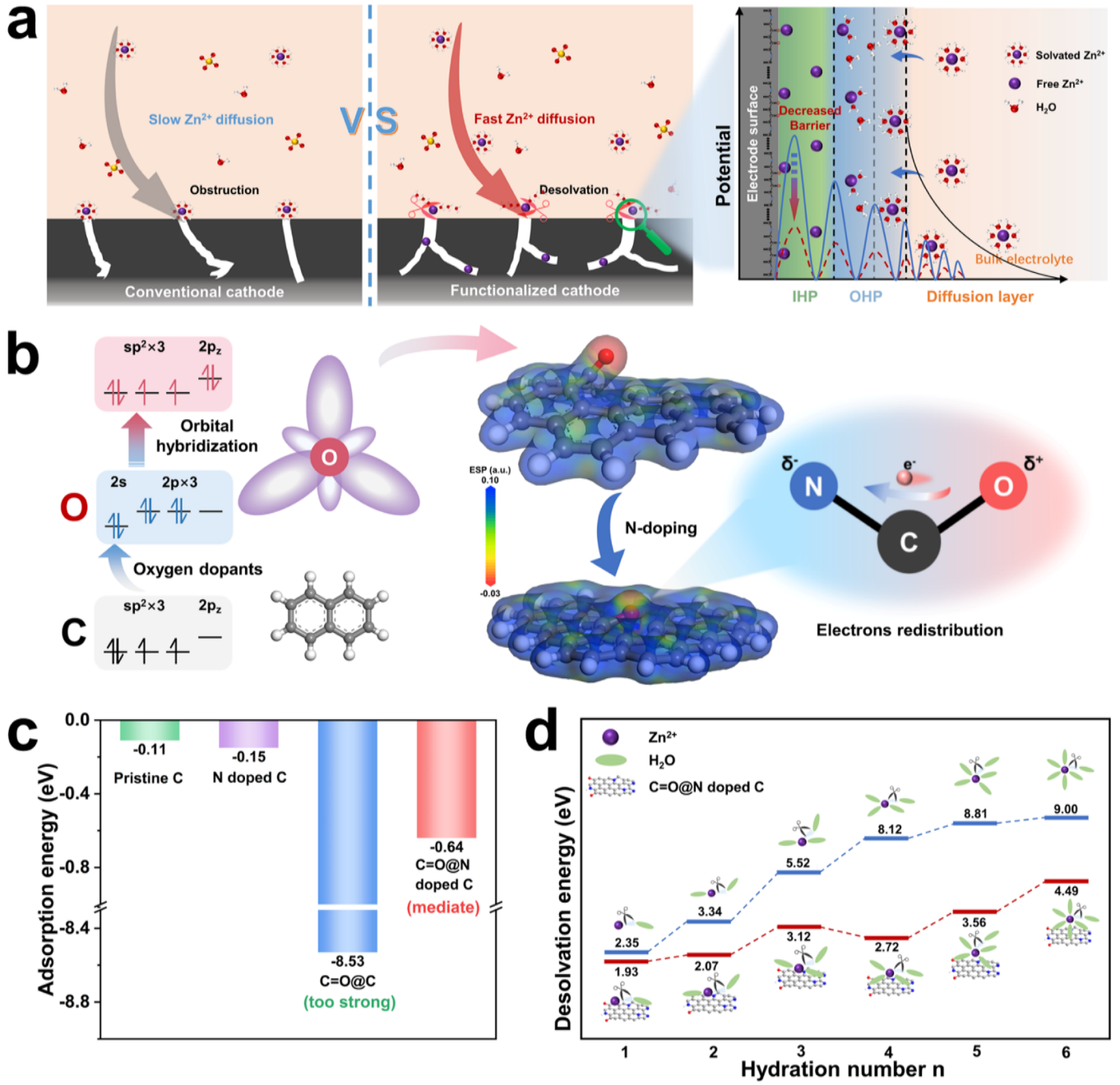

Fig. 1. (a) Schematic illustration of Zn^{2+} behavior on conventional and functionalized cathodes of ZIHCs. (b) Electrostatic potential of C O@C and C O@N doped C as well as schematic diagrams of oxygen orbital hybridization and electron redistribution. (c) The summary of adsorption energy of Zn^{2+} on the active sites of pristine C, N doped C, C O@C and C O@N doped C, respectively. (d) Comparison of desolvation energy barrier of $[Zn(H_2O)_n]^{2+}$ with different hydration numbers.

co-solvents. For example, the high-concentration electrolyte, ionic liquids and quasi-solid gel electrolytes can decrease the desolvation barrier by reducing the number of H_2O coordinated with Zn^{2+}, while the additives and co-solvents can replace the H_2O molecules in the $[Zn(H_2O)_6]^{2+}$ by organic molecule. However, their practical application is hindered by high cost, high viscosity and large ion transport resistance [21–23]. Alternatively, surface morphologies with tailored pore channels are designed to sieve the smaller $[Zn(H_2O)_n]^{2+}$ ($0 \leq n < 6$) species [24]. However, the pore sieving effect to physically separate coordinated H_2O from hydrated $[Zn(H_2O)_6]^{2+}$ relied mainly on the strength of electric fields to partially drive more Zn^{2+}-related species. The partially dissociated $[Zn(H_2O)_n]^{2+}$ reduces the amount of isolated Zn^{2+} at the interface, especially at low temperatures [25]. Similarly, near the conventional carbon/electrolyte interface, solvated Zn^{2+} clusters accumulate in the OHP (outer Helmholtz plane) layer by electrostatic interaction, and further diffuse into the IHP layer mainly by external electric field to overcome the large desolvation barriers, which severely limit the diffusion and storage of Zn^{2+} in kinetics. Theoretically, by constructing a functional catalytic interface with delocalized electrons, the strong interaction between the active sites and Zn^{2+} can reduce the desolvation energy barriers near the IHP and regulate the solvation shell behaviors, thus accelerating the desolvation kinetics and realizing efficient Zn^{2+} storage (Fig. 1a) [26–28]. Up to date, the electrocatalysis has been adopted to propel the dissociation of $Li(solvents)^+$ for generating more isolated Li^+ to facilitate the redox reaction or plating [29–32], but nobody knows how it works in the aqueous Zn-rated system such as ZIHCs. Therefore, designing catalytic electrodes with suitable pore morphology to modulate the hydrated $[Zn(H_2O)_6]^{2+}$ behaviors in the IHP would be beneficial for achieving high performance of ZIHCs.

Admittedly, the catalytic efficiency is related with the number of active sites, which is induced by the local electronic density redistribution [33,34]. Herein, differing from conventional architecture designing, the molecular orbitals of carbon electrodes with the co-existence of anionic oxygen and nitrogen are proposed to delocalize electrons *via* redistribution, generating more catalytic sites on the surface from the aspect of electronic density engineering. In detail, grafting oxygen and nitrogen atoms onto the carbon substrate pulls up the intrinsic *p*-band center of the carbon layer with excessive bonding ability, creating more delocalized electrons and controlling the bonding ability within a suitable range. As a demo, hierarchical pore channels decorated activated carbon microspheres (ACMs) with oxygen/nitrogen dopants are exampled to expedite the dissociation of $[Zn(H_2O)_6]^{2+}$ by pore and catalytic sieving, regulating the Zn^{2+} behaviors in the IHP layer. As comprehensively demonstrated *via* Raman and *in-situ* sum frequency generation (SFG) spectroscopies as well as theoretical simulations, the electrocatalytic sites are facilitated to liberate numerous Zn^{2+} from hydration sheath *via* reducing desolvation energy barriers, while the multilevel pore channels are assisted in sieving the large-sized solvated cations in advance. Besides, as revealed in electrochemical quartz crystal microbalance (EQCM), the catalytic desolvation behaviors and charge storage mechanism of the as-prepared electrode are systematically investigated, showing significant pseudo-capacitance property with the interaction of isolated Zn^{2+}. Consequently, the assembled ZIHCs exhibit a superior capacity of 177.2 mAh g^{-1}, corresponding to 158.8 Wh kg^{-1}, and provide an outstanding power density up to 15.7 kW kg^{-1}. Impressively, even under harsh condition (0°C) with severe solvation structure, the ZIHCs still deliver a fantastic capacity of 121.0 mAh g^{-1} and stabilize for 10000 cycles with a capacity retention of 99.42% at 5 A g^{-1}.

2. Results and discussion

Initially, the electronic distribution and possible dissociation behaviors of $[Zn(H_2O)_6]^{2+}$ on the N/O co-doped carbon were evaluated by density functional theory (DFT) calculation, respectively. As displayed in Fig. 1b, sp^2-hybrid oxygen atom doped at the edge of carbon matrix increases the local electron density, generating strong electron-donating carbonyl (C=O) group. However, with nitrogen doping, the electron redistribution leads to enhanced electron delocalization, weakening the electron density and forming more catalytic sites [35]. The adsorption energies of Zn^{2+} on carbon with/without dopants were further calculated in Fig. 1c. The C=O@C presents too strong adsorption energy for Zn^{2+} (-8.53 eV), trending to form stable chemical bonds to lead the loss of active sites. However, the C=O@N doped C exhibits moderate adsorption energy (-0.64 eV) in favor of reversible Zn^{2+} adsorption/-desorption, which is superior to pristine C (-0.11 eV) and N-doped C (-0.15 eV). Furthermore, the total density of states (DOS) in Fig. S1 also demonstrates that the C=O@C exhibits an extortionate *p*-band center (-1.73 eV) within powerful local electrons. The *s-p* hybridization is bounded to generate both bonding state (*s-p*) and antibonding state (*s-p**) and the extortionate p-band center would correspondingly shift antibonding *s-p** to higher energy region. Notably, the N/O co-doping leads to electron redistribution, which makes the C=O@N doped C with suitable *p*-band center of -2.53 eV, showing moderate bonding ability with Zn^{2+} [36]. As further elucidated in the partial density of state (Fig. S2a), the C $2p_z$ orbital electron delocalization is enhanced after heteroatom co-doping, enhancing the catalytic activity of the active sites [37,38]. Meanwhile, the O $2p_x$ orbital shows a peak of DOS at the Fermi level (Fig. S2b). The results indicate that the N-doping facilitates the migration of O $2p_x$ orbital electrons between active sites, reducing the activation energy of the adsorption reaction and improving the reversibility and structural stability of the active sites [39,40]. In addition, the desolvation energy barriers for the removal of active H_2O molecules from $[Zn(H_2O)_6]^{2+}$ with/without the influence of C=O@N doped C were calculated, respectively. As displayed in Fig. 1d, the gradual desolvation energy barrier of hydrated Zn^{2+} near the C=O@N doped C interface is significantly lower than before, conforming to above-mentioned forecast. For example, the energy required for dissociating $[Zn(H_2O)_6]^{2+}$ into isolated Zn^{2+} is 37.14 eV, whereas the energy required at the C=O@N doped C interface is only 17.89 eV. Based on the above results, the catalytic effect caused by electron density redistribution plays an important role in promoting the dissociation of $[Zn(H_2O)_6]^{2+}$ on the C=O@N doped C, which occurs in the IHP layer with forming more free Zn^{2+}.

According to the theoretical results, a N/O co-doped ACM material was designed and demoed as the electrode for ZIHCs, as illustrated in Fig. 2a. Briefly, the polymer microsphere precursors were synthesized *via* a micro-suspension polymerization between styrene and divinylbenzene, where the vinyl imidazole and paraffin served as the nitrogen source and the pore-forming agent, respectively. Through the air oxidation, carbonization and CO_2 activation, the N/O co-doped ACMs with abundant micro/meso-porous structure were achieved. Scanning electron microscopy (SEM) images of ACM-*x* (where *x* represents the percentage amount of paraffin) in Figs. 2b and S3 show good spherical morphology and narrow size distribution, indicating the perfectly inherited architecture from the precursors (Fig. S4). Additionally, the particle sizes of carbon are evaluated to be about 3-10 μm (Fig. S5), which is consistent with the SEM results. Moreover, transmission electron microscopy (TEM) image of ACM-40 clearly demonstrates the spherical shape without hollow structure (Fig. 2c). Abundant micropores and some mesopores are observed in the high-resolution TEM (HR-TEM) image of ACM-40 (Fig. 2d), which are in favor of promoting the pre-dissolution of hydrated ions and accelerating Zn ion diffusion [24, 41]. Noteworthily, no discernible lattice fringes are observed in the HR-TEM image while diffraction rings belonging to amorphous phase are observed in the selected electron diffraction (SAED) pattern, suggesting the amorphous structure [42]. Furthermore, the element mapping images (Fig. 2e) of ACM-40 confirm the homogeneous distribution of C, N, and O elements throughout the microspheres.

X-ray diffraction patterns in Fig. 2f clearly show a high strength at low angle and only a tiny wide peak at about 43° corresponding to the (100) plane, indicating the amorphous property [42]. The Raman

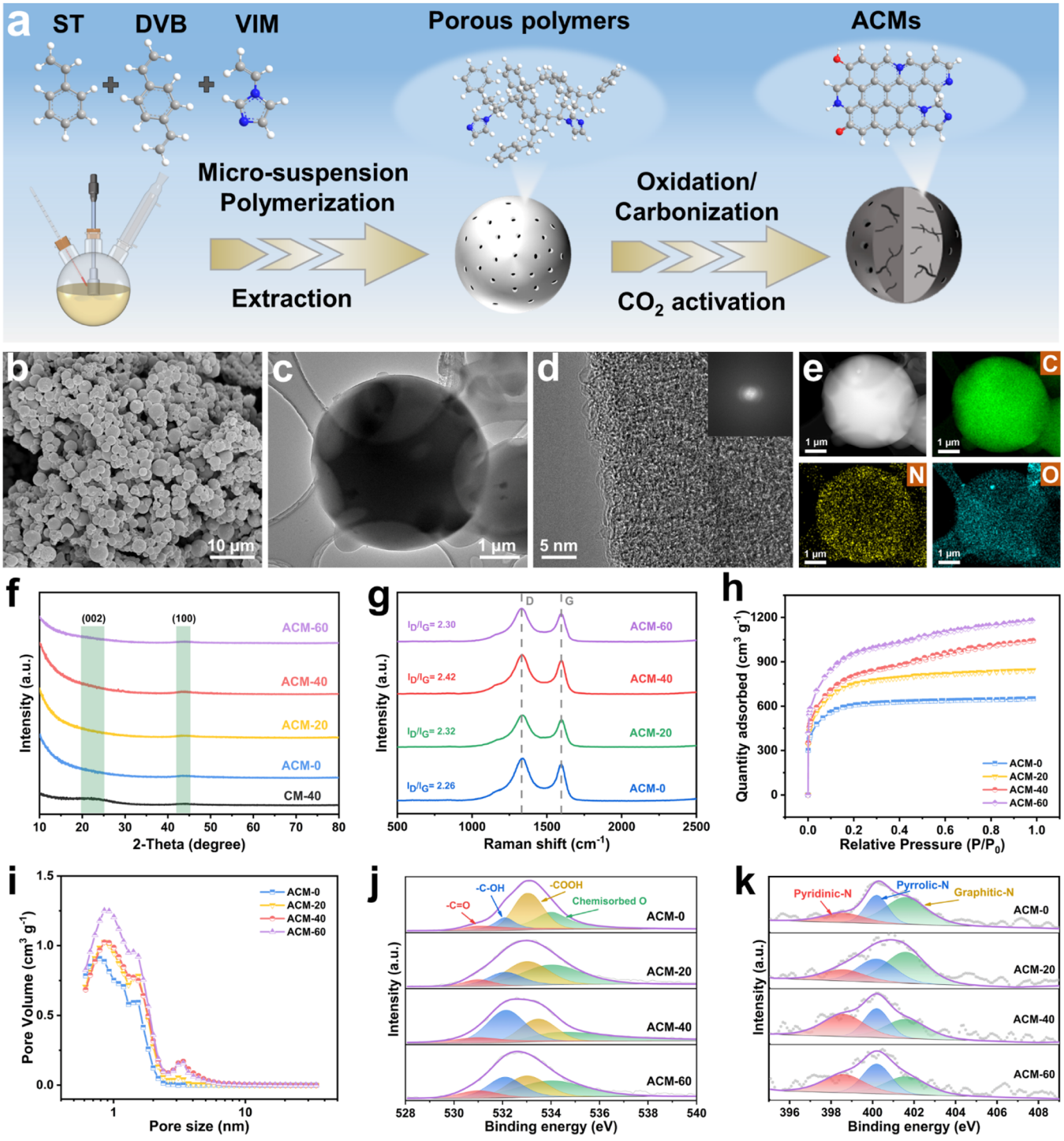

Fig. 2. (a) Schematic illustration of the preparation process of ACM-*x* samples. (b) SEM, (c) TEM, (d) HR-TEM images of ACM-40 with the corresponding SAED and (e) HAADF-TEM image and corresponding elemental mapping of ACM-40. (f) X-ray diffraction patterns of CM-40 and ACM-*x*, (g) Raman spectra of ACM-*x*, (h) Nitrogen adsorption/desorption isotherms, (i) pore-size distributions of AMC-*x*. High-resolution O 1s (j) and N 1s (k) X-ray photoelectron spectra of ACM-*x*.

spectra (Fig. 2g) reveal the ACM-40 with the largest value of I_D/I_G (2.42) and the smallest value of L_a (Figs. S6 and S7), indicating higher degree of disorder and more topological defects in the carbon lattices [11,43]. Further, the adsorption-desorption isotherm of microporous ACM-*x* series are investigated with H4-type hysteresis loops (Fig. 2h), indicating their hierarchical porous structure [44]. In addition, all the ACM-*x* samples have displayed the micro/meso-pores (Fig. 2i). Notably, as summarized in Table S1, the ACM-40 exhibits high specific surface area up to 2775.4 cm^2 g^{-1} and the highest meso-porosity ratio (39.89%), which is beneficial for the desolvation pathway [24]. Considering the ideal size of $[Zn(H_2O)_6]^{2+}$ (0.86 nm), the ACM-40 delivers the highest $S_{>0.86nm}/S_{BET}$ ratio of 66.48%, which significantly improves the utilization of electrochemical active sites [8]. To ascertain the chemical surroundings, X-ray photoelectron spectroscopy was further performed (Fig. S8). The O 1s spectrum can be fitted to four peaks of carbonyl (-C=O, 531.0 eV), carboxyl (-C-OH, 532.1 eV), carboxyl (-COOH, 533.0 eV) and chemisorbed oxygen (534.0 eV), respectively (Fig. 2j) [45]. Accordingly, the oxygen content in the ACM-40 sample is 3.84%

(Table S2) and the -C-OH accounts for the highest ratio. In addition, the ACM-40 sample also has the highest nitrogen content up to 1.31%, which exists in three forms of pyridinic-N (398.4 eV), pyrrolic-N (400.2 eV) and graphitic-N (402.0 eV) (Fig. 2k) [46]. Meanwhile, the Fourier transform infrared spectroscopy was also employed to investigate the ACM-40 surface functional groups, confirming the presence of nitrogen/oxygen functional groups (Fig. S9) [47]. The N/O co-doping heteroatoms not only regulate the space charge distribution of carbon matrix, but also boost the electrochemically active sites.

To verify the changes of solvation structure in the IHP, Raman spectra of ACM-40 electrode with commercial $ZnSO_4$ electrolyte were compared (Fig. 3a). Generally, the solvent separated ion pairs (SSIP, $[Zn^{2+}(H_2O)_6\ SO_4^{2}\ ]$) and contact ion pairs (CIP, $[Zn^{2+}(H_2O)_5\ OSO_3^{2}\ ]$) are existed in the bulk electrolyte[48]. A slight blue shift of the ν-SO_4^{2} occurs when introducing the ACM-40 into the system, corresponding to the conversion from SSIP to CIP [14]. The relative intensity of the HOH-OSO_3^{2} peak at the electrode/electrolyte interface of ACM-40 is enhanced in the solvation structure, implying an increase in the local Zn^{2+} concentration caused by catalytic desolvation at the interface [49]. Furthermore, the ACM-40 displays the smallest integrated area ratio (25.04, Fig. S10) of the ν-SO_4^{2} band and the ν-OH band [50], indicating the best desolvation effect.

Since the dissociation process occurs at the electrode/electrolyte interface, the interface-sensitive SFG is suitable for dynamically monitoring the dissociation behavior of $[Zn(H_2O)_6]^{2+}$ at the electrolyte/cathode interface by observing and probing the status of O-H band (Fig. 3b) [51,52]. The *in-situ* SFG is a second-order nonlinear optical technique that utilizes a visible and an infrared incident laser beam overlapping in an asymmetric interface region to generate a third beam (SFG signal) [53,54]. As illustrated in Fig. 3c, these observed peaks in the SFG of ACM-0 are attributed to ice-like water (tetrahedrally coordinated water molecules, ~3100 cm ^{1}), liquid-water (a more random arrangement, ~3300 cm ^{1}), material interface dangling O-H (~3500 cm ^{1}) and free O-H (water interface dangling, ~3700 cm ^{1}), respectively, indicating the presence of water solvents at the electrode/electrolyte interface.[51,53,55,56] Upon applying bias voltage of 40 mV, the signal of the O-H band in the free water is obviously enhanced, suggesting the accumulation of free water at the interface. Significantly,

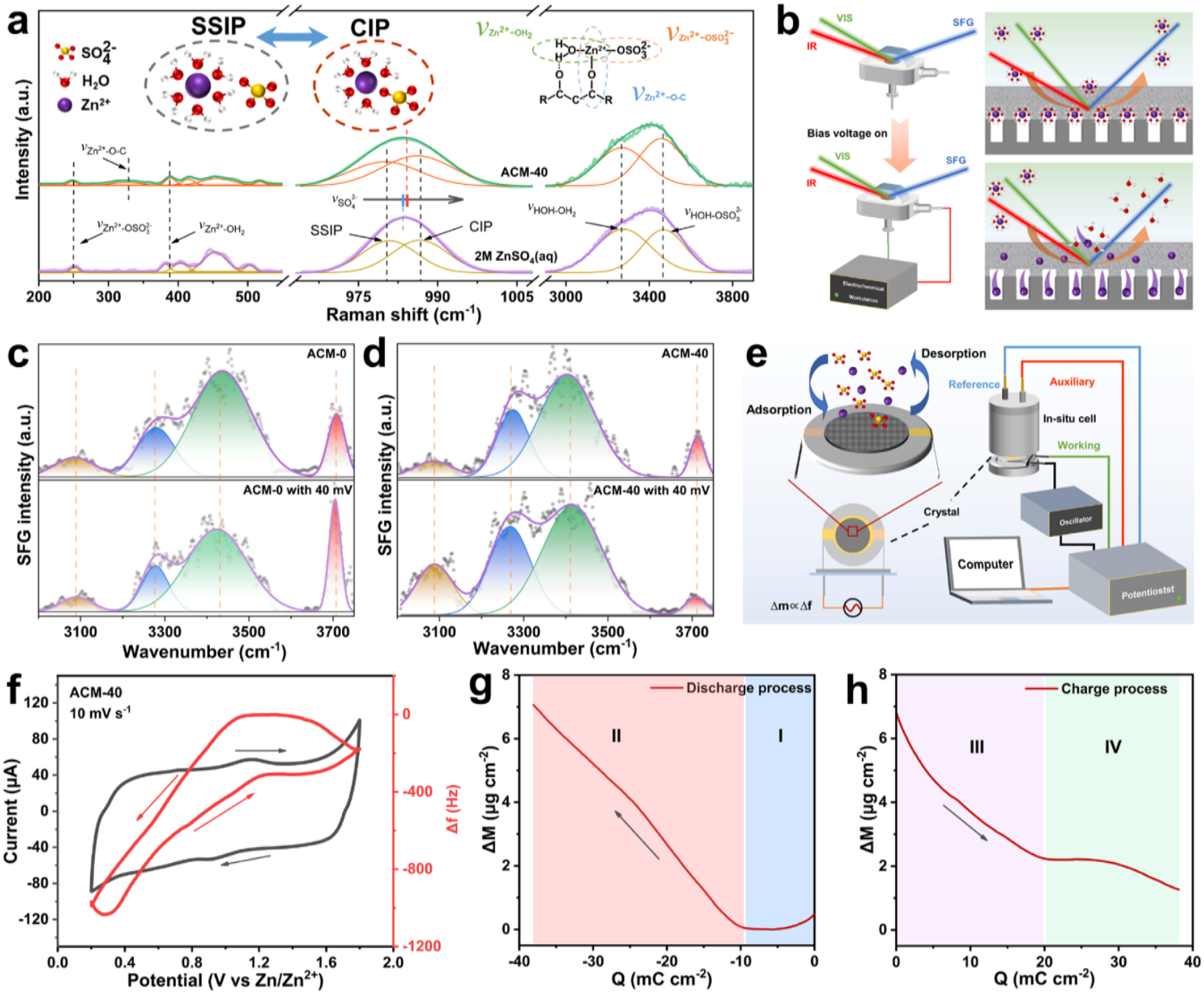

Fig. 3. (a) Raman spectra of pristine 2M $ZnSO_4$ solution with/without ACM-40 catalyst in electrolyte. (b) Schematic diagram of *in-situ* SFG probing the electrolyte/electrode interface as well as molecular states of the Zn^{2+} solvated structure with/without bias voltage. The intensity changes of SFG spectra of Zn^{2+} solvation structure on the (c) ACM-0 and (d) ACM-40 with/without the bias of 40 mV in the -OH region, respectively. (e) Schematic diagram of *in-situ* EQCM device. (f) CV curve at 10 mV s^{-1} and response to corresponding mass changes. The variation curve of mass with charge during (g) discharge and (h) charging processes, respectively.

as shown in the SFG spectrum of ACM-40 (Fig. 3d), the signal of O-H band in the free water almost disappears with the application of bias voltage, indicating the dissociation and dissipation of free water at the interface. In comparison, the SFG signal of ACM-20 does not change significantly, while the ACM-60 shows a similar trend to ACM-40 (Fig. S11), suggesting the fast desolvation with more catalytic sites and deep electronic delocalization.

Furthermore, an advanced electrogravimetric analysis for the ACM-40 cathode is further adopted by *in-situ* EQCM to study its electrochemical behavior through tracing the weight variation during charging and discharging processes (Fig. 3e). Combined with EQCM and *ex-situ* XRD, simultaneous mass changes on the ACM-40 cathode were sensitively recorded and clearly distinguished into four sections with significant differences on the types of adsorbent ions (Figs. 3f and S12) [57, 58]. As shown in Fig. 3g, the response curve of the mass change with charge during the discharging process can be divided into two regions "I" (1.8-1.1V) and "II" (1.1-0.2V). The decrease of mass in region "I" with the accumulation of charge is attributed to the adsorption of Zn^{2+} derived from the solvation shell. The mass of the cathode in region "II" increases rapidly with the accumulation of charge, which corresponds to the precipitation of $Zn_4SO_4(OH)_6\ 5H_2O$, the adsorption of Zn^{2+}/H^+ and the desorption of SO_2^4 [8]. In addition, as shown in Fig. 3h, the response curve of mass change with charge during the charging process can also be distinguished into two regions "III" (0.2-1.23V) and "IV" (1.23-1.8V). The mass of the region "III" decreases rapidly with the accumulation of charge due to the dissolution of $Zn_4SO_4(OH)_6\ 5H_2O$ and the desorption of Zn^{2+}/H^+. The mass of the cathode in the region "IV" decreases slowly with the accumulation of charge, corresponding to the desorption of Zn^{2+} and SO_2^4 [50]. The *in-situ* EQCM experiment results show that Zn^{2+} cations derived from the $[Zn(H_2O)_6]^{2+}$ participate in the reversible chemisorption reaction of the ACM-40 cathode, improving the pseudo-capacitance and charge storage capacity of ZIHCs.

Based on the fast desolvation promotion by catalytic and pore sieving, the electrochemical properties of assembled ZIHCs (denoted as ACM-*x*//Zn) were further evaluated (Fig. 4a). Firstly, a large potential difference is observed in the cyclic voltammetry (CV) curves of the ZIHCs (Fig. S13), indicating a wide voltage window of ACM-40//Zn [59]. Both the CV curves (Fig. S14) and galvanostatic charge-discharge (GCD) curves (Fig. S15) of ACM-40//Zn demonstrate typical pseudo-capacitive energy storage mechanism induced by the N/O doping [60]. Notably, the CV curve of ACM-40//Zn exhibits the largest integrated area, demonstrating the highest capacitive performance. The ACM-40//Zn ZIHC possesses the largest specific capacitance of 177.2 mAh g^{-1} at 0.1 A g^{-1}, surpassing the other ACM-*x*//Zn systems. Even enhancing to 20 A g^{-1}, a high capacity of 90.7 mAh g^{-1} is achieved (Fig. 4b). Besides, the Nyquist plot of the ACM-40 shows the smallest charge transfer resistance than those of the other samples (Fig. S16), indicating its stronger charge transfer capacity and lower diffusion barriers. After fitting the experimental results (Fig. S17 and S18), the activation energy of the ACM-40 cathode is calculated to be 13.00 kJ mol^{-1} according to the Arrhenius equation, which is lower than others, indicating that the ACM-40 cathode has the greater ability to remove the Zn^{2+} from the solvation sheath and promote ion transfer kinetics. Additionally, as shown in Fig. 4c, ACM-40 presents the smallest Warburg coefficient (σ) value, suggesting the fastest Zn^{2+} diffusion kinetics in ACM-40. Through the $i = av^b$ equation where *i* is the peak current and *ν* is the sweep rate, the calculated b values of ACM-40 are 0.896 (the reduction peaks) and 0.946 (the oxidization peaks), respectively, indicating its mainly capacitive reaction with fast electrochemical kinetics (Fig. S19) [61]. Moreover, according to the Dunn method ($i = k_1v + k_2v^{0.5}$), the diffusion behavior contribution is also considerable, even up to 37% at 5 mV s^{-1} (Fig. 4d), indicating its superior pseudo-capacitance [62].

To further evaluate the potential for practical application, different mass loading ACM-40 cathodes were investigated. The ACM-40//Zn with 12 mg cm^{-2} still displays 93.1 mAh g^{-1} (Fig. S20). As expected, the ACM-40//Zn also provided a battery-level energy density of 158.78 Wh kg^{-1} at a power density of 92.40 W kg^{-1}, and maintained a high energy density of 70.21 Wh kg^{-1} even at a high power density of 15.7 kW kg^{-1}, significantly superior to other reported carbon-based ZIHCs (Fig. S21) [63–67]. In practical applications, ZIHCs suffer from the severe challenge of larger solvation shell under low temperature environment, where the ionic conductivity drops sharply with the decreased temperature. As shown in Fig. 4e, the ACM-40//Zn operating at 0°C delivers a desirable specific capacity of 121.0 mAh g^{-1} at 0.1 A g^{-1}. Meanwhile, the ACM-40//Zn displays impressive rate behaviors and achieves a noteworthy capacity of 74.6 mAh g^{-1} when subjected to a current density of 20 A g^{-1} under 0°C, which is superior to the electrochemical performance of commercial activated carbon YP-50F at 25°C. Finally, the ACM-40//Zn discloses high-capacity retentions of 95.73% and 99.42% after 10000 cycles at 5 A g^{-1} under 25 or 0°C, respectively (Figs. 4f and S22). Both Coulombic efficiencies were close to 100%, showing outstanding cyclic stability and wide operating temperature range. The surprising low-temperature electrochemical properties are attributed to the rapid ion diffusion kinetics accelerated by the fast desolvation process at the surface of ACM-40 cathode.

To verify the flexibility of ACM-40 materials, a flexible quasi-solid-state ZIHC with polyacrylamide/$ZnSO_4$ gel as the electrolyte was further assembled. A high open-circuit voltage of 1.30 V is remained after resting for 500 h, indicating its outstanding self-discharge resistance capability (Figs. 4g and S23). Moreover, the quasi-solid-state ZIHC exhibited excellent rate performance in Fig. 4h, where a maximum specific capacity of 173.0 mAh g^{-1} was obtained at 0.1 A g^{-1} and a reversible specific capacity of 41.7 mAh g^{-1} was presented even at 20 A g^{-1}. When the assembled quasi-solid-state ZIHC was bent at different angles or multiple times at 90°, the CV curves experienced little change, demonstrating an excellent flexibility and reversibility (Fig. S24). Fig. 4i shows the quasi-solid-state ZIHCs exhibit a high energy density of 154.46 Wh kg^{-1} and a high power density of 7.3 kW kg^{-1}, making it an excellent candidate to drive the lights or smart devices (Fig. 4h inset). It is significant to point out the improvement over previously reported quasi-solid-state ZIHCs [63–66,68]. Consistently, the quasi-solid-state ZIHC stabilizes the capacity retention rate of 92.62% at 5 A g^{-1} and Coulombic efficiency as high as 100% after 10000 cycles (Fig. S25). These results demonstrate the pore and catalytic sieving in regulating IHP for practical application.

3. Conclusion

In summary, to regulate the Zn^{2+} behaviors in the IHP layer, the dissociation of $[Zn(H_2O)_6]^{2+}$ for accelerating Zn^{2+} diffusion kinetics is realized by coupling pore sieving and electrocatalysis on the N/O co-doped ACM electrode with multilevel channels, serving as an catalytic accelerator. The catalytic desolvation mechanism of the designed electrode is comprehensively investigated by *in-situ* electrochemical characterizations and theoretical simulations. As a result, the obtained multifunctional cathode enables the ZIHCs with an outstanding capacity of 177.2 mAh g^{-1} and a power density up to 15.7 kW kg^{-1}. Even operating at harsh condition (0°C) with severe solvation structure, the ZIHC still delivers a fantastic capacity of 121.0 mAh g^{-1} and stabilizes for 10000 cycles with a capacity retention of 99.42% at 5 A g^{-1}. This work provides a feasible strategy for enhancing the Zn^{2+} storage capability of electrode by simultaneously catalyzing and sieving the solvation structure of Zn^{2+}, raising a bright way to achieve high-performance Zn-related electrochemical systems.

CRediT authorship contribution statement

Ziling Wu: Writing – review & editing, Writing – original draft, Investigation, Data curation, Conceptualization. **Yinze Zuo:** Writing – review & editing, Writing – original draft, Software, Methodology,

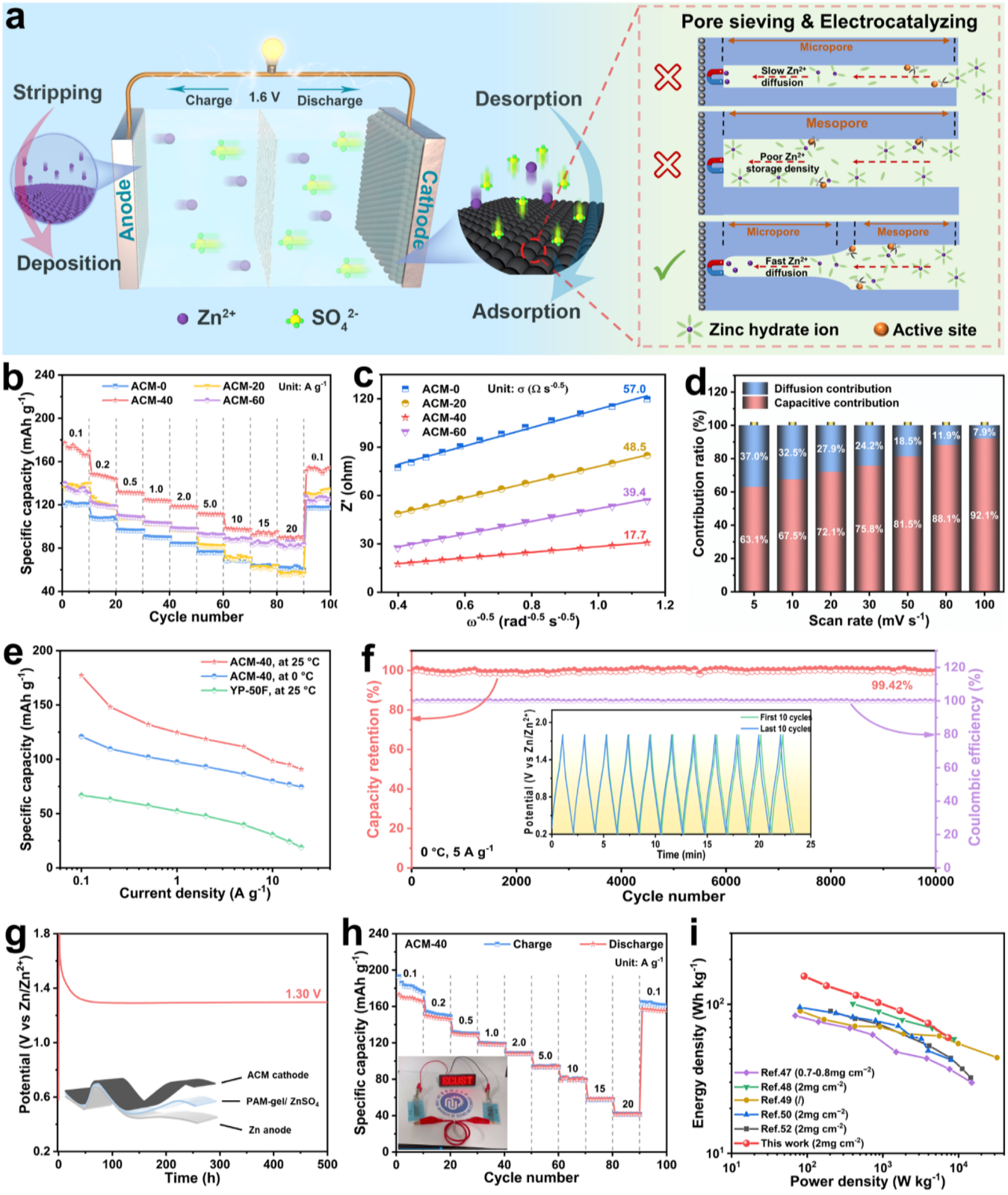

Fig. 4. (a) Schematic illustration of configuration and working mechanism of the as-made aqueous ZIHCs. (b) Rate capabilities of aqueous ZIHCs. (c) Relationships between Z′ and $\omega^{-0.5}$. (d) Normalized contribution ratios of charge capacity stored by capacitive process and diffusion-controlled process of the ACM-40 cathode at different sweep rates. (e) Comparison on rate capabilities of ACM-40 cathode at 25°C and extremely low temperatures. (f) Cyclabilities of ACM-40//Zn at 5 A g^{-1} and 0°C (insets are the GCD curves of initial ten cycles and last ten cycles). (g) Self-discharge curve and (h) rate capabilities of the as-assembled quasi-solid-state ZIHCs. (i) Ragone plots of the as-assembled quasi-solid-state ZIHCs and other quasi-solid-state ZIHCs previously reported.

Formal analysis, Data curation. **Yongzheng Zhang:** Supervision. **Xiang Li:** Software. **Jing Zhang:** Resources. **Yanli Wang:** Funding acquisition. **Chunyin Shen:** Project administration. **Xiaomin Cheng:** Methodology. **Meinan Liu:** Funding acquisition. **Haitao Liu:** Formal analysis. **Hongzhen Lin:** Funding acquisition. **Jian Wang:** Writing – review & editing, Writing – original draft, Supervision, Funding acquisition, Conceptualization. **Liang Zhan:** Writing – review & editing, Writing – original draft, Validation, Supervision, Funding acquisition, Conceptualization. **Licheng Ling:** Funding acquisition.

Declaration of competing interest

The authors declare that they have no known competing financial interests or personal relationships that could have appeared to influence the work reported in this paper.

Data availability

Data will be made available on request.

Acknowledgements

Z. W. and Y. Z. contributed equally to this work. This work was financially supported by the National Key R&D Program of China (2021YFA1201503), the National Natural Science Foundation of China (Nos. 21972164, 22279161, 12264038, 22309144, 22075081, 11874089), the Natural Science Foundation of Jiangsu Province (BK. 20210130), the Innovative and Entrepreneurial Doctor in Jiangsu Province (JSSCBS20211428), the China Postdoctoral Science Foundation (No. 2023M732561, 2023M731084), the Pilot Group Program of the Research Fund for International Senior Scientists (No. 22250710676), the Shanghai Sailing Program of China (23YF1408900) and the Fundamental Research Funds for the Central Universities (JKD01231701). J. W. acknowledged the funding provided by the Alexander von Humboldt Foundation and the basic funding of the Helmholtz Association. Dr. Y. Z. Zhang thanks the Shanghai Super Postdoctoral Incentive Program. We also thank the support from Nano-X, Suzhou Institute of Nano-tech and Nano-bionics, Chinese Academy of Sciences.

References

[1] A. Hauch, R. Küngas, P. Blennow, A.B. Hansen, J.B. Hansen, B.V. Mathiesen, M. B. Mogensen, Recent advances in solid oxide cell technology for electrolysis, Science 370 (6513) (2020) eaba6118, https://doi.org/10.1126/science.aba6118.

[2] G. Li, L. Sun, S. Zhang, C. Zhang, H. Jin, K. Davey, G. Liang, S. Liu, J. Mao, Z. Guo, Developing cathode materials for aqueous zinc ion batteries: challenges and practical prospects, Adv. Funct. Mater. (2023) 2301291, https://doi.org/10.1002/adfm.202301291.

[3] D. Zhang, L. Li, Y. Gao, Y. Wu, J. Deng, Carbon-based materials for a new type of zinc-ion capacitor, ChemElectroChem 8 (9) (2021) 1541–1557, https://doi.org/10.1002/celc.202100282.

[4] J. Yin, W. Zhang, N.A. Alhebshi, N. Salah, H.N. Alshareef, Electrochemical zinc ion capacitors: fundamentals, materials, and systems, Adv. Energy Mater. 11 (21) (2021) 2100201, https://doi.org/10.1002/aenm.202100201.

[5] M.S. Javed, T. Najam, I. Hussain, M. Idrees, A. Ahmad, M. Imran, S.S.A. Shah, R. Luque, W. Han, Fundamentals and scientific challenges in structural design of cathode materials for zinc-ion hybrid supercapacitors, Adv. Energy Mater. (2022) 2202303, https://doi.org/10.1002/aenm.202202303.

[6] J. Jin, X. Geng, Q. Chen, T. Ren, A better Zn-ion storage device: recent progress for Zn-ion hybrid supercapacitors, Nano-Micro Lett. 14 (1) (2022) 64, https://doi.org/10.1007/s40820-022-00793-w.

[7] Y. Zhang, C. Zhu, Y. Xiong, Z. Gao, W. Hu, J. Shi, J. Chen, W. Tian, J. Wu, M. Huang, H. Wang, Multi-channel hollow carbon nanofibers with graphene-like shell-structure and ultrahigh surface area for high-performance Zn-ion hybrid capacitors, Small Methods (2023) 2300714, https://doi.org/10.1002/smtd.202300714.

[8] L. Wang, M. Peng, J. Chen, T. Hu, K. Yuan, Y. Chen, Eliminating the micropore confinement effect of carbonaceous electrodes for promoting Zn-ion storage capability, Adv. Mater. 34 (39) (2022) 2203744, https://doi.org/10.1002/adma.202203744.

[9] R. Yuan, H. Wang, L. Shang, R. Hou, Y. Dong, Y. Li, S. Zhang, X. Chen, H. Song, Revealing the self-doping defects in carbon materials for the compact capacitive energy storage of Zn-ion capacitors, ACS Appl. Mater. Interfaces 15 (2) (2023) 3006–3016, https://doi.org/10.1021/acsami.2c19798.

[10] W. Lu, B. Xie, C. Yang, C. Tian, L. Yan, J. Ning, S. Li, Y. Zhong, Y. Hu, Phosphorus-mediated local charge distribution of N-configuration adsorption sites with enhanced zincophilicity and hydrophilicity for high-energy-density Zn-ion hybrid supercapacitors, Small 19 (45) (2023) 2302629, https://doi.org/10.1002/smll.202302629.

[11] Z. Peng, A.G. Bannov, S. Li, Y. Huang, L. Tang, L. Tan, Y. Chen, Coupling uniform pore size and multi-chemisorption sites: hierarchically ordered porous carbon for ultra-fast and large zinc ion storage, Adv. Funct. Mater. 33 (40) (2023) 2303205, https://doi.org/10.1002/adfm.202303205.

[12] Y. Wang, S. Sun, X. Wu, H. Liang, W. Zhang, Status and opportunities of zinc ion hybrid capacitors: focus on carbon materials, current collectors, and separators, Nano-Micro Lett. 15 (1) (2023) 78, https://doi.org/10.1007/s40820-023-01065-x.

[13] Y. Liu, L. Wu, Recent advances of cathode materials for zinc-ion hybrid capacitors, Nano Energy 109 (2023) 108290, https://doi.org/10.1016/j.nanoen.2023.108290.

[14] T. Wang, P. Wang, L. Pan, Z. He, L. Dai, L. Wang, S. Liu, S.C. Jun, B. Lu, S. Liang, J. Zhou, Stabling zinc metal anode with polydopamine regulation through dual effects of fast desolvation and ion confinement, Adv. Energy Mater. 13 (5) (2023) 2203523, https://doi.org/10.1002/aenm.202203523.

[15] P. Hu, X. Luo, T. Hu, S. Chen, D. Li, Y. Chen, F. Li, Ethanol solvent used in constructing ultra-low-temperature zinc-ion capacitors with a long cycling life, ACS Appl. Mater. Interfaces 15 (4) (2023) 5180–5190, https://doi.org/10.1021/acsami.2c19041.

[16] L. Jia, H. Hu, X. Cheng, H. Dong, H. Li, Y. Zhang, H. Zhang, X. Zhao, C. Li, J. Zhang, H. Lin, J. Wang, Toward low-temperature zinc-ion batteries: strategy, progress, and prospect in vanadium-based cathodes, Adv. Energy Mater. (2023) 2304010, https://doi.org/10.1002/aenm.202304010.

[17] J. Huang, H. Liang, Y. Tang, B. Lu, J. Zhou, S. Liang, *In situ* induced coordination between a "Desiccant" interphase and oxygen-deficient navajoite towards highly efficient zinc ion storage, Adv. Energy Mater. 12 (35) (2022) 2201434, https://doi.org/10.1002/aenm.202201434.

[18] J. Cao, D. Zhang, X. Zhang, Z. Zeng, J. Qin, Y. Huang, Strategies of regulating Zn^{2+} solvation structures for dendrite-free and side reaction-suppressed zinc-ion batteries, Energy Environ. Sci. 15 (2) (2022) 499–528, https://doi.org/10.1039/D1EE03377H.

[19] S. Zhang, M. Ye, Y. Zhang, Y. Tang, X. Liu, C.C. Li, Regulation of ionic distribution and desolvation activation energy enabled by *in situ* zinc phosphate protective layer toward highly reversible zinc metal anodes, Adv. Funct. Mater. 33 (22) (2023) 2208230, https://doi.org/10.1002/adfm.202208230.

[20] Y. Zhang, Z. Cao, S. Liu, Z. Du, Y. Cui, J. Gu, Y. Shi, B. Li, S. Yang, Charge-enriched strategy based on MXene-based polypyrrole layers toward dendrite-free zinc metal anodes, Adv. Energy Mater. 12 (13) (2022) 2103979, https://doi.org/10.1002/aenm.202103979.

[21] Z. Chang, H. Yang, Y. Qiao, X. Zhu, P. He, H. Zhou, Tailoring the solvation sheath of cations by constructing electrode front-faces for rechargeable batteries, Adv. Mater. 34 (34) (2022) 2201339, https://doi.org/10.1002/adma.202201339.

[22] D. Xiao, L. Zhang, Z. Li, H. Dou, X. Zhang, Design strategies and research progress for Water-in-Salt electrolytes, Energy Storage Mater. 44 (2022) 10–28, https://doi.org/10.1016/j.ensm.2021.09.035.

[23] J. Han, A. Mariani, M. Zarrabeitia, Z. Jusys, R.J. Behm, A. Varzi, S. Passerini, Zinc-ion hybrid supercapacitors employing acetate-based water-in-salt electrolytes, Small 18 (31) (2022) 2201563, https://doi.org/10.1002/smll.202201563.

[24] Z. Lu, C. Geng, H. Yang, P. He, S. Wu, Q. Yang, H. Zhou, Step-by-step desolvation enables high-rate and ultra-stable sodium storage in hard carbon anodes, Proc. Natl. Acad. Sci. 119 (40) (2022) e2210203119, https://doi.org/10.1073/pnas.2210203119.

[25] Q. Ma, R. Gao, Y. Liu, H. Dou, Y. Zheng, T. Or, L. Yang, Q. Li, Q. Cu, R. Feng, Z. Zhang, Y. Nie, B. Ren, D. Luo, X. Wang, A. Yu, Z. Chen, Regulation of outer solvation shell toward superior low-temperature aqueous zinc-ion batteries, Adv. Mater. 34 (49) (2022) 2207344, https://doi.org/10.1002/adma.202207344.

[26] S. Tu, B. Zhang, Y. Zhang, Z. Chen, X. Wang, R. Zhan, Y. Ou, W. Wang, X. Liu, X. Duan, L. Wang, Y. Sun, Fast-charging capability of graphite-based lithium-ion batteries enabled by Li3P-based crystalline solid–electrolyte interphase, Nat. Energy 8 (12) (2023) 1365–1374, https://doi.org/10.1038/s41560-023-01387-5.

[27] L. Jia, H. Hu, X. Cheng, H. Dong, H. Li, Y. Zhang, H. Zhang, X. Zhao, C. Li, J. Zhang, H. Lin, J. Wang, Toward low-temperature zinc-ion batteries: strategy, progress, and prospect in vanadium-based cathodes, Adv. Energy Mater. 14 (8) (2024) 2304010, https://doi.org/10.1002/aenm.202304010.

[28] G. Duan, Y. Wang, B. Luo, L. Sun, S. Zheng, J. Huang, Z. Ye, Taurine-mediated dynamic bridging strategy for highly stable Zn metal anode, Energy Storage Mater. 61 (2023) 102882, https://doi.org/10.1016/j.ensm.2023.102882.

[29] J. Wang, L. Li, H. Hu, H. Hu, Q. Guan, M. Huang, L. Jia, H. Adenusi, K.V. Tian, J. Zhang, S. Passerini, H. Lin, Toward dendrite-free metallic lithium anodes: from structural design to optimal electrochemical diffusion kinetics, ACS Nano 16 (11) (2022) 17729–17760, https://doi.org/10.1021/acsnano.2c08480.

[30] J. Wang, J. Zhang, S. Duan, L. Jia, Q. Xiao, H. Liu, H. Hu, S. Cheng, Z. Zhang, L. Li, W. Duan, Y. Zhang, H. Lin, Lithium atom surface diffusion and delocalized deposition propelled by atomic metal catalyst toward ultrahigh-capacity dendrite-free lithium anode, Nano Lett. 22 (19) (2022) 8008–8017, https://doi.org/10.1021/acs.nanolett.2c02611.

[31] L. Li, H. Tu, J. Wang, M. Wang, W. Li, X. Li, F. Ye, Q. Guan, F. Zhu, Y. Zhang, Y. Hu, C. Yan, H. Lin, M. Liu, Electrocatalytic MOF-carbon bridged network accelerates Li +-solvents desolvation for high Li+ diffusion toward rapid sulfur redox kinetics, Adv. Funct. Mater. 33 (13) (2023) 2212499, https://doi.org/10.1002/adfm.202212499.

[32] J. Wang, J. Zhang, S. Cheng, J. Yang, Y. Xi, X. Hou, Q. Xiao, H. Lin, Long-life dendrite-free lithium metal electrode achieved by constructing a single metal atom anchored in a diffusion modulator layer, Nano Lett. 21 (7) (2021) 3245–3253, https://doi.org/10.1021/acs.nanolett.1c00534.

[33] P. Chen, T. Wang, D. He, T. Shi, M. Chen, K. Fang, H. Lin, J. Wang, C. Wang, H. Pang, Delocalized isoelectronic heterostructured FeCoOxSy catalysts with tunable electron density for accelerated sulfur redox kinetics in Li-S batteries, Angew. Chem. Int. Ed. 62 (47) (2023) e202311693, https://doi.org/10.1002/anie.202311693.

[34] J. Wang, L. Jia, J. Zhong, Q. Xiao, C. Wang, K. Zang, H. Liu, H. Zheng, J. Luo, J. Yang, H. Fan, W. Duan, Y. Wu, H. Lin, Y. Zhang, Single-atom catalyst boosts electrochemical conversion reactions in batteries, Energy Storage Mater. 18 (2019) 246–252, https://doi.org/10.1016/j.ensm.2018.09.006.

[35] C. Hu, L. Dai, Doping of carbon materials for metal-free electrocatalysis, Adv. Mater. 31 (7) (2019) 1804672, https://doi.org/10.1002/adma.201804672.

[36] Q. Wang, J. Su, H. Chen, D. Wang, X. Tian, Y. Zhang, X. Feng, S. Wang, J. Li, H. Jin, Highly conductive nitrogen-doped sp2/sp3 hybrid carbon as a conductor-free charge storage host, Adv. Funct. Mater. 32 (51) (2022) 2209201, https://doi.org/10.1002/adfm.202209201.

[37] J. Zhang, C. You, H. Lin, J. Wang, Electrochemical kinetic modulators in lithium–sulfur batteries: from defect-rich catalysts to single atomic catalysts, Energy Environ. Mater. 5 (3) (2022) 731–750, https://doi.org/10.1002/eem2.12250.

[38] J. Zhang, R. He, Q. Zhuang, X. Ma, C. You, Q. Hao, L. Li, S. Cheng, L. Lei, B. Deng, X. Li, H. Lin, J. Wang, Tuning 4f-center electron structure by Schottky defects for catalyzing Li diffusion to achieve long-term dendrite-free lithium metal battery, Adv. Sci. 9 (23) (2022) 2202244, https://doi.org/10.1002/advs.202202244.

[39] W. Zhang, J. Yin, W. Jian, Y. Wu, L. Chen, M. Sun, U. Schwingenschlögl, X. Qiu, H. N. Alshareef, Supermolecule-mediated defect engineering of porous carbons for zinc-ion hybrid capacitors, Nano Energy 103 (2022) 107827, https://doi.org/10.1016/j.nanoen.2022.107827.

[40] S. Kang, D. Choi, H. Lee, B. Choi, Y. Kang, A mechanistic insight into the oxygen redox of Li-rich layered cathodes and their related electronic/atomic behaviors upon cycling, Adv. Mater. 35 (43) (2023) 2211965, https://doi.org/10.1002/adma.202211965.

[41] F. Mo, Y. Wang, T. Song, X. Wu, Nitrogen and oxygen co-doped hierarchical porous carbon for zinc-ion hybrid capacitor, J. Energy Storage 72 (2023) 108228, https://doi.org/10.1016/j.est.2023.108228.

[42] H. Wang, M. Wang, Y. Tang, A novel zinc-ion hybrid supercapacitor for long-life and low-cost energy storage applications, Energy Storage Mater. 13 (2018) 1–7, https://doi.org/10.1016/j.ensm.2017.12.022.

[43] Z. Pei, Q. Meng, L. Wei, J. Fan, Y. Chen, C. Zhi, Toward efficient and high rate sodium-ion storage: a new insight from dopant-defect interplay in textured carbon anode materials, Energy Storage Mater. 28 (2020) 55–63, https://doi.org/10.1016/j.ensm.2020.02.033.

[44] H. Adelkhani, The effect of acidity of electrolyte on the porosity and the nanostructure morphology of electrolytic manganese dioxide, Appl. Surf. Sci. 258 (17) (2012) 6232–6238, https://doi.org/10.1016/j.apsusc.2012.02.146.

[45] D. Hulicova-Jurcakova, M. Seredych, G.Q. Lu, T.J. Bandosz, Combined effect of nitrogen- and oxygen-containing functional groups of microporous activated carbon on its electrochemical performance in supercapacitors, Adv. Funct. Mater. 19 (3) (2009) 438–447, https://doi.org/10.1002/adfm.200801236.

[46] L. Liu, B. Du, R. Liu, X. Chen, H. Song, N-doped hierarchically porous carbon aerogels by controlling the Zn-chitosan complex ratio for high-performance supercapacitors, Energy Fuels 36 (11) (2022) 5920–5927, https://doi.org/10.1021/acs.energyfuels.2c00512.

[47] R. Atchudan, T.N.J.I. Edison, Y.R. Lee, Nitrogen-doped carbon dots originating from unripe peach for fluorescent bioimaging and electrocatalytic oxygen reduction reaction, J. Colloid Interface Sci. 482 (2016) 8–18, https://doi.org/10.1016/j.jcis.2016.07.058.

[48] W. Yang, Y. Yang, H. Yang, H. Zhou, Regulating water activity for rechargeable zinc-ion batteries: progress and perspective, ACS Energy Lett. 7 (8) (2022) 2515–2530, https://doi.org/10.1021/acsenergylett.2c01152.

[49] H. Yang, Y. Qiao, Z. Chang, H. Deng, X. Zhu, R. Zhu, Z. Xiong, P. He, H. Zhou, Reducing water activity by zeolite molecular sieve membrane for long-life rechargeable zinc battery, Adv. Mater. 33 (38) (2021) 2102415, https://doi.org/10.1002/adma.202102415.

[50] C. Zhao, Y. Lin, Q. Lin, Q. Liu, Y. Liu, Z. Liu, A. Ying, C-P/C=O bonds assisted desolvation effect in ultra-micropores carbon for boosting Zn-ion storage capability, Energy Storage Mater. 58 (2023) 332–343, https://doi.org/10.1016/j.ensm.2023.03.039.

[51] T. Li, J. Wang, Y. Xu, Y. Cao, H. Lin, T. Zhang, Hierarchical structure formation and effect mechanism of Ni/Mn layered double hydroxides microspheres with large-scale production for flexible asymmetric supercapacitors, ACS Appl. Energy Mater. 1 (5) (2018) 2242–2253, https://doi.org/10.1021/acsaem.8b00321.

[52] J. Wang, J. Zhang, J. Wu, M. Huang, L. Jia, L. Li, Y. Zhang, H. Hu, F. Liu, Q. Guan, M. Liu, H. Adenusi, H. Lin, S. Passerini, Interfacial "Single-Atom-in-Defects" catalysts accelerating Li+ desolvation kinetics for long-lifespan lithium metal batteries, Adv. Mater. 35 (39) (2023) 2302828, https://doi.org/10.1002/adma.202302828.

[53] Y. Xu, Y. Ma, F. Gu, S. Yang, C. Tian, Structure evolution at the gate-tunable suspended graphene–water interface, Nature 621 (2023) 506, https://doi.org/10.1038/s41586-023-06374-0.

[54] A. Myalitsin, S.H. Urashima, S. Nihonyanagi, S. Yamaguchi, T. Tahara, Water structure at the buried silica/aqueous interface studied by heterodyne-detected vibrational sum-frequency generation, J. Phys. Chem. C 120 (17) (2016) 9357–9363, https://doi.org/10.1021/acs.jpcc.6b03275.

[55] K. Niu, R.A. Marcus, Sum frequency generation, calculation of absolute intensities, comparison with experiments, and two-field relaxation-based derivation, Proc. Natl. Acad. Sci. 117 (6) (2020) 2805–2814, https://doi.org/10.1073/pnas.1906243117.

[56] S. Yamaguchi, Y. Suzuki, Y. Nojima, T. Otosu, Perspective on sum frequency generation spectroscopy of ice surfaces and interfaces, Chem. Phys. 522 (2019) 199–210, https://doi.org/10.1016/j.chemphys.2019.03.005.

[57] J. Chen, L. Wang, M. Peng, T. Hu, K. Yuan, Y. Chen, Zinc-ion capacitors with fast kinetics at a high mass loading, Chem. Mater. 35 (10) (2023) 4089, https://doi.org/10.1021/acs.chemmater.3c00563.

[58] K. Ge, H. Shao, E. Raymundo-Piñero, P.L. Taberna, P. Simon, Cation desolvation-induced capacitance enhancement in reduced graphene oxide (rGO), Nat. Commun. 15 (1) (2024) 1935, https://doi.org/10.1038/s41467-024-46280-1.

[59] J. Huang, K. Yuan, Y. Chen, Wide voltage aqueous asymmetric supercapacitors: advances, strategies, and challenges, Adv. Funct. Mater. 32 (4) (2022) 2108107, https://doi.org/10.1002/adfm.202108107.

[60] X. Han, X. Kong, D. Wang, X. Li, L. Dong, Hydrous ruthenium oxide quantum dots anchored on carbon nanocages for Zn-ion hybrid capacitors, Chem. Eng. J. 477 (2023) 147078, https://doi.org/10.1016/j.cej.2023.147078.

[61] F. Wei, H. Zhang, X. Hui, Y. Lv, S. Ran, X. Liu, N doped porous carbon nanosheets with enhanced zinc ion storage capability, J. Power Sources 554 (2023) 232348, https://doi.org/10.1016/j.jpowsour.2022.232348.

[62] T. Brezesinski, J. Wang, S.H. Tolbert, B. Dunn, Ordered mesoporous α-MoO3 with iso-oriented nanocrystalline walls for thin-film pseudocapacitors, Nat. Mater. 9 (2) (2010) 146–151, https://doi.org/10.1038/nmat2612.

[63] L. Dong, X. Ma, Y. Li, L. Zhao, W. Liu, J. Cheng, C. Xu, B. Li, Q. Yang, F. Kang, Extremely safe, high-rate and ultralong-life zinc-ion hybrid supercapacitors, Energy Storage Mater. 13 (2018) 96–102, https://doi.org/10.1016/j.ensm.2018.01.003.

[64] X. Ma, J. Cheng, L. Dong, W. Liu, J. Mou, L. Zhao, J. Wang, D. Ren, J. Wu, C. Xu, F. Kang, Multivalent ion storage towards high-performance aqueous zinc-ion hybrid supercapacitors, Energy Storage Mater. 20 (2019) 335–342, https://doi.org/10.1016/j.ensm.2018.10.020.

[65] K. Shang, Y. Liu, P. Cai, K. Li, Z. Wen, N, P, and S co-doped 3D porous carbon-architectured cathode for high-performance Zn-ion hybrid capacitors, J. Mater. Chem. A 10 (12) (2022) 6489–6498, https://doi.org/10.1039/D2TA00202G.

[66] T. Song, H. Hao, Y. Zhao, X. Wang, C. Li, W. Li, High-performance Zn-ion hybrid supercapacitor enabled by the hierarchical N/S co-doped graphene/polyaniline cathode, J. Alloys Compd. 924 (2022) 166493, https://doi.org/10.1016/j.jallcom.2022.166493.

[67] J. Li, J. Zhang, L. Yu, J. Gao, X. He, H. Liu, Y. Guo, G. Zhang, Dual-doped carbon hollow nanospheres achieve boosted pseudocapacitive energy storage for aqueous zinc ion hybrid capacitors, Energy Storage Mater. 42 (2021) 705–714, https://doi.org/10.1016/j.ensm.2021.08.018.

[68] X. Zhu, F. Guo, C. Ji, H. Mi, C. Liu, J. Qiu, Nitrogen-doped hollow carbon nanoboxes in zwitterionic polymer hydrogel electrolyte for superior quasi-solid-state zinc-ion hybrid supercapacitors, J. Mater. Chem. A 10 (24) (2022) 12856–12868, https://doi.org/10.1039/D2TA02449G.